

Magnetization-direction-tunable kagome Weyl line

Zi-Jia Cheng^{*†1}, Ilya Belopolski^{*1}, Tyler A. Cochran^{*1}, Hung-Ju Tien^{*2}, Xian P. Yang^{*1}, Wenlong Ma³, Jia-Xin Yin¹, Junyi Zhang⁴, Chris Jozwiak⁵, Aaron Bostwick⁵, Eli Rotenberg⁵, Guangming Cheng⁶, Md. Shafayat Hossain¹, Qi Zhang¹, Nana Shumiya¹, Daniel Multer¹, Maksim Litskevich¹, Yuxiao Jiang¹, Nan Yao⁶, Biao Lian⁴, Guoqing Chang⁷, Shuang Jia³, Tay-Rong Chang^{†2}, M. Zahid Hasan^{†1,8}

1. Laboratory for Topological Quantum Matter and Advanced Spectroscopy (B7), Department of Physics, Princeton University, Princeton, NJ, USA
2. Department of Physics, National Cheng Kung University, Tainan, Taiwan
3. International Center for Quantum Materials, School of Physics, Peking University, Beijing, China
4. Department of Physics, Princeton University, Princeton, New Jersey 08544, USA
5. Advanced Light Source, E. O. Lawrence Berkeley National Laboratory, Berkeley, California 94720, USA
6. Princeton Institute for Science and Technology of Materials, Princeton University, Princeton, NJ, USA
7. Division of Physics and Applied Physics, School of Physical and Mathematical Sciences, Nanyang Technological University, 21 Nanyang Link, 637371, Singapore
8. Lawrence Berkeley National Laboratory, Berkeley, CA 94720, USA

Kagome magnets provide a fascinating platform for a plethora of topological quantum phenomena. Here, utilizing angle-resolved photoemission spectroscopy, we demonstrate Weyl lines with strong out-of-plane dispersion in an A-A stacked kagome magnet $Tb_xGd_{1-x}Mn_6Sn_6$. On the Gd rich side, the Weyl line remains nearly spin-orbit-gapless due to a remarkable cooperative interplay between Kane-Mele spin-orbit-coupling, low site symmetry and in-plane magnetic order. Under Tb substitution, the kagome Weyl line gaps due to a magnetic reorientation to out-of-plane order. Our results illustrate the magnetic moment direction as an efficient tuning knob for realizing distinct three-dimensional topological phases.

† zijiac@princeton.edu, u32trc00@phys.ncku.edu.tw, mzhasan@princeton.edu

Topological quantum magnets can host electronic structures with Dirac and Weyl points and lines near the Fermi level, which are effective in concentrating Berry curvature in bulk momentum space [1–6]. This large Berry curvature, in turn, has been observed to drive giant anomalous Hall and Nernst effects [7–13], even up to room temperature [14–16], making these exotic magnets promising candidates for magnetic field sensors [10,17], thermoelectric converters [14,18] and Berry curvature memories [19,20]. Manipulation of the global topology and Berry curvature geometry in such magnetic semimetals promises to enable new exotic response and device functionality, but remains experimentally challenging. While magnetic topological insulators have long been manipulated by doping and gating to obtain exotic topological states [21–24], known room temperature topological magnetic semimetals are three-dimensional bulk with comparatively high carrier density. The manipulation of the intrinsic bulk magnetic order offers a new design principle for next-generation field-free topological engineering, but has been little studied [25,26].

The kagome lattice exhibits frustration and two-dimensional Dirac points, suggesting that stacked kagome materials may naturally allow magnetic tunability of electronic topology [6,27–33]. Recently, RMn_6Sn_6 (R is a rare Earth) has emerged as a versatile family of kagome magnets offering rich magnetic orders with different rare earth element R [34,35], critical temperatures above room temperature and a topological Chern gap arising from a spin-orbit gapped kagome Dirac point [4]. For example, $GdMn_6Sn_6$ is an easy-plane ferrimagnet with a Curie temperature $T_C \sim 440$ K [35,36], while $TbMn_6Sn_6$ is an easy-axis ferrimagnet with $T_C \sim 420$ K [35]. Substituting Gd with Tb in alloy $Tb_xGd_{1-x}Mn_6Sn_6$ can further smoothly tune the magnetic ground state without introducing impurity on Mn kagome layer [[37], also see Figs.S3-4 in [39]], offering an attractive platform for understanding the interplay between magnetic momentum direction and topological electronic structure. Moreover, deviating from ideal quasi-2D kagome model, the low anisotropy in resistivity and highly three-dimensional character of *ab initio* electronic structure calculations [36] suggests a significant interlayer coupling, motivating investigation of three-dimensional topology in RMn_6Sn_6 emerging from the A-A stacked Mn lattice. Here we employ angle-resolved photoemission spectroscopy (ARPES) to probe the three-dimensional electronic structure of $Tb_xGd_{1-x}Mn_6Sn_6$, providing the evidence, for the first time, of three-dimensional magnetic nodal lines near the Fermi level (E_f) with magnetization-direction tunable spin-orbit coupling (SOC) gap in RMn_6Sn_6 .

Ultraviolet ARPES measurements were performed at beamline 5.2 in the Stanford Synchrotron Light Source (SSRL), beamline 7.0.2 in the Advanced Light Source (ALS) and Bloch beamline in the MAX IV. The energy (angle resolution) was better than 20meV (0.2 degree), respectively. Soft X-ray (SX) ARPES data was collected at the ADDRESS beamline at Switzerland Light Source (SLS) [38], with 150meV energy resolution at 650eV photon energy. Samples were cleaved and measured between 10K and 20K. The details of sample preparation, TEM, magnetization characterization and calculation can be found in [39].

$GdMn_6Sn_6$ has a layered hexagonal crystal structure (P6/mmm) [37]. The unit cell exhibits a stacking pattern R-M-S1-S2-S1-M-R along the c direction, where R, M, S1, S2 represent $GdSn_2$ honeycomb layers, Mn kagome layers, Sn hexagonal layers and Sn honeycomb layers, respectively [Fig. 1(a,b)]. The two clean Mn kagome layers in one unit cell form a simple A-A stacking with

interlayer separation close to $c/2$, in sharp contrast to other well-studied kagome magnets such as Fe_3Sn_2 [8], Mn_3Sn [7] and $\text{Co}_3\text{Sn}_2\text{S}_2$ [10]. At low temperature, GdMn_6Sn_6 shows in-plane ferrimagnetic order, but upon substitutional Tb doping ($\text{Tb}_{0.2}\text{Gd}_{0.8}\text{Mn}_6\text{Sn}_6$) exhibits a magnetic reorientation transition to an out-of-plane easy axis [Figs. 1(c), S2 [39], [37]].

We first examine our GdMn_6Sn_6 samples by high-resolution ARPES on the (001) cleaving plane at incident photon energy 140 eV with linear horizontal (LH) polarization and the results are shown in Figs. 1(e,f). The spectra readily reveal a cone dispersion at the \bar{K} point of the surface Brillouin zone (BZ) with crossing point energy $E_D = -(0.04 \pm 0.01)$ eV and Fermi velocity $v_{KK} = (6.7 \pm 0.8) \times 10^4$ m/s⁻¹. This Fermi velocity is significantly smaller than that of graphene, but typical among transition metal kagome magnets [4,28], suggesting a Dirac cone state arising from localized 3d electrons on the Mn kagome lattice. Since the system is ferrimagnetic, the electronic structure is generically singly- degenerate and these Dirac cones are spin-polarized.

Having observed the Dirac cone state originating from the two-dimensional kagome sheets, we next consider the evolution of this electronic structure in three-dimensional momentum space. We first acquire an ARPES photon energy dependence to probe the electronic structure at different k_z [Fig. 2(a)]. Surprisingly, for the state indicated by the green arrows, we observe a clear oscillation of intensity with a periodicity of $4\pi/c$, doubling the expected $2\pi/c$ periodicity of the nominal bulk BZ. This oscillation indicates a doubling of the effective BZ, or halving of the effective crystallographic unit cell [Fig. 2(b), in the following we will adopt the notation of doubled BZ for the high symmetry points]. To further explore this BZ doubling effect, we examine the electronic structure at $k_z = 9\frac{2\pi}{c}$ ($h\nu = 140$ eV) and $k_z = 10\frac{2\pi}{c}$ ($h\nu = 172$ eV). In the nominal BZ, these two k_z both correspond to Γ , but now in the doubled BZ they correspond to the Γ -K-M and A_u - H_u - L_u planes, respectively. Zooming in on the FS at $k_z = 9\frac{2\pi}{c}$ shown in Fig 2(c), we observe that the upper branch of the Dirac state, labelled D_1 , appears as a crescent-moon-shaped pocket centered at H_u . Mimicking graphene [40] and FeSn [28], the observed pattern is consistent with sublattice interference of the lattice-driven nodal state and a manifestation of the π Berry phase of the wavefunction [39,41,42]. In contrast, at $k_z = 10\frac{2\pi}{c}$ the circular Dirac pocket increases in size and its distribution of spectral weight changes dramatically [Fig. 2(f)]. Moreover, the K-K' cut exhibits hole-like linearly dispersing bands [Fig. 2(g)]. The full dispersion is well captured by a fit to a minimal kagome model, which is shown as dashed line in Fig. 2(g), suggesting a kagome Dirac crossing point (label D_2) at 130 meV above E_F . We observe that the Fermi velocity of D_2 is nearly twice that of D_1 , indicating distinct Mn orbital origins for the D_1 and D_2 kagome Dirac cones [also see Figs. S7-8]. To understand the interplay between the Mn kagome Dirac cones and doubled BZ, we note that the conventional unit cell contains two Mn kagome planes, with almost equal intra-unit-cell distance (4.51Å) and inter-unit-cell distance (4.49Å), naturally halving the effective crystallographic unit cell [left panel in Fig. 2(b)]. As the states with energy near E_f are mainly from Mn 3d orbitals [Fig. S11 [39]], the observed zone-selective behavior of the states can be understood as an interference effect from the electrons emitting from adjacent kagome planes, which carries phase information of the initial states [39]. We further support this interpretation by band unfolded Green's function *ab initio* calculations, which capture both the observed dispersion

and spectral weight distribution observed by photoemission for alternating n [Figs. 2(e,h)]. The clear BZ doubling with alternating appearance of distinct Dirac states indicates the bulk nature of the kagome Dirac cones, and further points to a significant coupling between Mn kagome layers, suggesting an emergent three-dimensional magnetic topological state.

To probe the evolution of the kagome Dirac states in the stacking direction, we explore our GdMn₆Sn₆ samples by bulk sensitive soft-X-ray ARPES(SX-ARPES). We acquire a photon energy dependence to extract the $E - k_z$ dispersion along K-H_u [Fig. 3(a), Fig. S10-11 [39]], which cuts through the D₁ kagome Dirac cone. Remarkably, we observe a considerable out-of-plane k_z bandwidth of 120 meV for the kagome Dirac state, with the band top at H_u and the band bottom near H. We further acquire conventional ARPES spectra on the (100) side surface to more directly probe, without photon energy dependence, the $E - k_z$ dispersion through D₂ [Fig. 3(b)]. Again we observe a large k_z bandwidth of 230 meV, suggestive of a strongly out-of-plane dispersive kagome Dirac state. The k_z dispersion for both three-dimensional Dirac cone structures quantitatively agrees with our band-unfolded *ab initio* calculations shown in Fig. 3(c). Our k_z resolved photoemission spectra suggest that under interlayer coupling the D₁ and D₂ kagome Dirac cones independently form emergent three-dimensional magnetic nodal structures with large k_z dispersion.

To more deeply understand the magnetic nodal structure, we examine our *ab initio* calculation along K-H_u without SOC. We find that the two-fold degeneracy of D₁ is preserved along the entire K-H_u path of the bulk BZ, forming a magnetic nodal line structure which can be understood as a natural consequence of the A-A stacking of kagome sheets [Fig. 3(c) inset]. Including SOC in our calculation, we find that the induced gap remains extremely small, < 0.5 meV, along the full trajectory of the nodal line [Fig. 4(f)]. By contrast, other kagome magnets, such as Fe₃Sn₂ [8] and TbMn₆Sn₆ [4], exhibit a moderate SOC gap of ~ 30 meV. The small SOC gap can be understood as arising from cooperative interplay between low site symmetry and in-plane magnetic order. First, the low site symmetry lifts the degeneracy of all $3d$ orbitals, suppressing on-site SOC. The next leading contribution is the inter-site Kane-Mele coupling, $H_{KM} \propto J_z S_z$, where J_z and S_z are the out-of-plane components of the orbital and spin angular momenta, respectively. However, the Kane-Mele SOC term is also strongly suppressed under the in-plane magnetic order of GdMn₆Sn₆, resulting in negligible S_z . The interplay of A-A kagome stacking, low site symmetry and in-plane magnetic order naturally produces a Weyl line with near-two-fold degeneracy in GdMn₆Sn₆.

Having provided evidence for a kagome Weyl line in GdMn₆Sn₆, we next explore magnetically tuning this topological electronic structure. We investigate Tb_{0.2}Gd_{0.8}Mn₆Sn₆, with out-of-plane magnetic order, by ARPES near H_u. In GdMn₆Sn₆, on an $E-k_x$ cut through the D₁ kagome Weyl line, we observe the expected linear dispersion, with one cone branch suppressed due to sublattice interference [Fig. 4(a)]. Interestingly, in contrast to the gapless dispersion in GdMn₆Sn₆, the same cut in Tb_{0.2}Gd_{0.8}Mn₆Sn₆ exhibits strongly suppressed spectral weight near the crossing point, indicating the existence of a gap [Figs. 4(b)]. We can directly identify the gap on an energy distribution curve (EDC) through H_u for Tb_{0.2}Gd_{0.8}Mn₆Sn₆ [Figs. 4(c), S13 [39]]. Fitting by two Lorentzian peaks yields a gap size $\Delta = (25 \pm 6)$ meV, of the same order of magnitude as the

kagome Dirac cone gap observed in Fe_3Sn_2 [8]. By contrast, the corresponding EDC for undoped GdMn_6Sn_6 is well-fit by a single Lorentzian peak. Corresponding *ab initio* calculations with in-plane magnetic moment exhibit a near-gapless Weyl line [Fig. 4(d)]. While under out-of-plane magnetic order, the Weyl line develops an SOC gap [Fig. 4(e)]. This out-of-plane SOC gap persists along the full Weyl line trajectory, with the largest splitting at H_u [Figs. 4(g)], suggesting enhanced Kane-Mele SOC associated with the out-of-plane magnetic order. Since the kagome Weyl line disperses close to the Fermi level, Berry curvature generated through the Kane-Mele SOC and concentrated along the Weyl line is expected to contribute to an enhanced AHE under out-of-plane magnetism [Fig. S14 [39]]. Taken together, our photoemission spectra and *ab initio* results unambiguously suggest the observation of a magnetically tunable Kane-Mele SOC gap in a kagome Weyl line.

Our systematic ARPES measurements and *ab initio* calculations reveal strongly three-dimensional magnetic Weyl lines originating from the A-A stacked Mn kagome lattice in $(\text{Tb,Gd})\text{Mn}_6\text{Sn}_6$, which was previously considered to be a quasi-two-dimensional system [4,34]. Moreover, we report, for the first time, that the Weyl line exhibits a strongly magnetization-direction tunable Kane-Mele SOC gap and Berry curvature distribution. Under in-plane magnetic order the gap is negligible, while under out-of-plane order the gap is strongly enhanced, consistent with a leading Kane-Mele SOC contribution. Our results point to the crucial role of magnetization direction and interlayer coupling in the topological electronic structure of RMn_6Sn_6 family and provide a general design principle for nodal lines with tunable mass and Berry curvature geometry. Since the magnetic reorientation transition in $(\text{Tb,Gd})\text{Mn}_6\text{Sn}_6$ can be tuned to room temperature, the Berry curvature concentrated by the Weyl line may allow the implementation a novel room-temperature anomalous Hall sensor with unusual directional sensitivity [34].

Reference:

- [1] N. P. Armitage, E. J. Mele, and A. Vishwanath, Weyl and Dirac semimetals in three-dimensional solids. *Rev. Mod. Phys.* **90**, 015001 (2018).
- [2] M. Z. Hasan *et al.*, Discovery of Weyl Fermion Semimetals and Topological Fermi Arc States. *Annu. Rev. Condens. Matter Phys.* **8**, 289 (2017).
- [3] D. N. Basov, R. D. Averitt, and D. Hsieh, Towards properties on demand in quantum materials. *Nat. Mater.* **16**, 1077 (2017).
- [4] J.-X. Yin *et al.*, Quantum-limit Chern topological magnetism in TbMn_6Sn_6 . *Nature* **583**, 533 (2020).
- [5] I. Belopolski *et al.*, Discovery of topological Weyl fermion lines and drumhead surface states in a room temperature magnet. *Science* **365**, 1278 (2019).
- [6] J.-X. Yin *et al.*, Negative flat band magnetism in a spin-orbit-coupled correlated kagome magnet. *Nat. Phys.* **15**, 443 (2019).
- [7] K. Kuroda *et al.*, Evidence for magnetic Weyl fermions in a correlated metal. *Nat. Mater.* **16**, 1090 (2017).
- [8] L. Ye *et al.*, Massive Dirac fermions in a ferromagnetic kagome metal. *Nature* **555**, 638 (2018).
- [9] D. S. Sanchez *et al.*, Observation of Weyl fermions in a magnetic non-centrosymmetric crystal. *Nat. Commun* **11**, 3356 (2020).
- [10] E. Liu *et al.*, Giant anomalous Hall effect in a ferromagnetic kagome-lattice semimetal. *Nat. Phys.* **14**, 1125 (2018).
- [11] D. Xiao, M.-C. Chang, and Q. Niu, Berry phase effects on electronic properties. *Rev. Mod. Phys.* **82**, 1959 (2010).
- [12] M. Ikhlas *et al.*, Large anomalous Nernst effect at room temperature in a chiral antiferromagnet. *Nat. Phys.* **13**, 1085 (2017).
- [13] S. Nakatsuji, N. Kiyohara, and T. Higo, Large anomalous Hall effect in a non-collinear antiferromagnet at room temperature. *Nature* **527**, 212 (2015).
- [14] A. Sakai *et al.*, Giant anomalous Nernst effect and quantum-critical scaling in a ferromagnetic semimetal. *Nat. Phys.* **14**, 1119 (2018).
- [15] X. Li *et al.*, Anomalous Nernst and Righi-Leduc Effects in Mn_3Sn : Berry Curvature and Entropy Flow. *Phys. Rev. Lett.* **119**, 056601 (2017).
- [16] T. Matsuda *et al.*, Room-temperature terahertz anomalous Hall effect in Weyl antiferromagnet Mn_3Sn thin films. *Nat. Commun* **11**, 909 (2020).
- [17] T. Suzuki *et al.*, Singular angular magnetoresistance in a magnetic nodal semimetal. *Science* **365**, 377 (2019).
- [18] A. Sakai *et al.*, Iron-based binary ferromagnets for transverse thermoelectric conversion. *Nature* **581**, 53 (2020).
- [19] A. Gao *et al.*, Layer Hall effect in a 2D topological axion antiferromagnet. *Nature* **595**, 521 (2021).
- [20] J. Xiao *et al.*, Berry curvature memory through electrically driven stacking transitions. *Nat. Phys.* **16**, 1028 (2020).
- [21] S.-Y. Xu *et al.*, Hedgehog spin texture and Berry's phase tuning in a magnetic topological insulator. *Nat. Phys.* **8**, 616 (2012).

- [22] C.-Z. Chang *et al.*, Experimental Observation of the Quantum Anomalous Hall Effect in a Magnetic Topological Insulator. *Science* **340**, 167 (2013).
- [23] I. Belopolski *et al.*, A novel artificial condensed matter lattice and a new platform for one-dimensional topological phases. *Sci. Adv.* **3**, e1501692 (2017).
- [24] Y. Tokura, K. Yasuda, and A. Tsukazaki, Magnetic topological insulators. *Nat. Rev. Phys.* **1**, 126 (2019).
- [25] A. Biswas *et al.*, Spin-Reorientation-Induced Band Gap in Fe_3Sn_2 : Optical Signatures of Weyl Nodes. *Phys. Rev. Lett.* **125**, 076403 (2020).
- [26] S. Nie *et al.*, Magnetic Semimetals and Quantized Anomalous Hall Effect in EuB_6 . *Phys. Rev. Lett.* **124**, 076403 (2020).
- [27] J.-X. Yin *et al.*, Giant and anisotropic many-body spin-orbit tunability in a strongly correlated kagome magnet. *Nature* **562**, 91 (2018).
- [28] M. Kang *et al.*, Dirac fermions and flat bands in the ideal kagome metal FeSn . *Nat. Mater.* **19**, 163 (2020).
- [29] G. Xu, B. Lian, and S.-C. Zhang, Intrinsic Quantum Anomalous Hall Effect in the Kagome Lattice $\text{Cs}_2\text{LiMn}_3\text{F}_{12}$. *Phys. Rev. Lett.* **115**, 186802 (2015).
- [30] S. S. Zhang *et al.*, Many-Body Resonance in a Correlated Topological Kagome Antiferromagnet. *Phys. Rev. Lett.* **125**, 046401 (2020).
- [31] Z. Lin *et al.*, Flatbands and Emergent Ferromagnetic Ordering in Fe_3Sn_2 Kagome Lattices. *Phys. Rev. Lett.* **121**, 096401 (2018).
- [32] Z. Guguchia *et al.*, Tunable anomalous Hall conductivity through volume-wise magnetic competition in a topological kagome magnet. *Nat. Commun* **11**, 559 (2020).
- [33] Y.-X. Jiang *et al.*, Unconventional chiral charge order in kagome superconductor KV_3Sb_5 . *Nat. Mater.* (2021).
- [34] W. Ma *et al.*, Rare Earth Engineering in RMn_6Sn_6 ($\text{R} = \text{Gd} - \text{Tm}, \text{Lu}$) Topological Kagome Magnets. *Phys. Rev. Lett.* **126**, 246602 (2021).
- [35] G. Venturini, B. C. E. Idrissi, and B. Malaman, Magnetic properties of RMn_6Sn_6 ($\text{R} = \text{Sc}, \text{Y}, \text{Gd}-\text{Tm}, \text{Lu}$) compounds with HfFe_6Ge_6 type structure. *J. Magn. Magn. Mater.* **94**, 35 (1991).
- [36] T. Asaba *et al.*, Anomalous Hall effect in the kagome ferrimagnet GdMn_6Sn_6 . *Phys. Rev. B* **101**, 174415 (2020).
- [37] N. V. Baranov, E. G. Gerasimov, and N. V. Mushnikov, Magnetism of compounds with a layered crystal structure. *Phys. Met. Metallogr.* **112**, 711 (2011).
- [38] V. N. Strocov *et al.*, Soft-X-ray ARPES facility at the ADDRESS beamline of the SLS: concepts, technical realisation and scientific applications. *J. Synchrotron Radiat.* **21**, 32 (2014).
- [39] See the Supplemental Material for additional information of methods and materials.
- [40] E. L. Shirley *et al.*, Brillouin-zone-selection effects in graphite photoelectron angular distributions. *Phys. Rev. B* **51**, 13614 (1995).
- [41] M. Mucha-Kruczyński *et al.*, Characterization of graphene through anisotropy of constant-energy maps in angle-resolved photoemission. *Phys. Rev. B* **77**, 195403 (2008).
- [42] I. Gierz *et al.*, Illuminating the dark corridor in graphene: Polarization dependence of angle-resolved photoemission spectroscopy on graphene. *Phys. Rev. B* **83**, 121408 (2011).

Acknowledgements:

The material characterization (ARPES) is supported by the United States Department of Energy (US DOE) under the Basic Energy Sciences program (grant number DOE/BES DE-FG-02-05ER46200). This research used resources of the Advanced Light Source(ALS), a DOE Office of Science User Facility under contract number DE-AC02-05CH11231. Use of the Stanford Synchrotron Radiation Light Source (SSRL), SLAC National Accelerator Laboratory, is supported by the U.S. Department of Energy, Office of Science, Office of Basic Energy Sciences, under contract no. DE-AC02-76SF00515. The authors thank Donghui Lu and Makoto Hashimoto at Beamline 5.2 of the SSRL for support. The authors thank C. Polley, J.Adell and B. Thiagarajan at Beamline Bloch of the Max IV, Lund, Sweden for support. The authors also thank V. Stokov and N. Schröter at Beamline ADDRESS of the Swiss Light Source (SLS) at Paul Scherrer Institut, Switzerland for support. The authors also want to thank J. Denlinger at Beamline 4.0.3(MERLIN) of the ALS for support in getting the preliminary data. The authors also acknowledge use of Princeton University's Imaging and Analysis Center, which is partially supported by the Princeton Center for Complex Materials (PCCM), a National Science Foundation (NSF)-MRSEC program (DMR-2011750). I.B. acknowledges the generous support of the Special Postdoctoral Researchers Program, RIKEN during the late stages of this work. T.A.C. acknowledges the support of the National Science Foundation Graduate Research Fellowship Program (DGE-1656466). B. L. acknowledges support from the Alfred P. Sloan Foundation. G.C. would like to acknowledge the support of the National Research Foundation, Singapore under its NRF Fellowship Award (NRF-NRFF13-2021-0010) and the Nanyang Assistant Professorship grant from Nanyang Technological University. T.-R.C. was supported by the Young Scholar Fellowship Program from the Ministry of Science and Technology (MOST) in Taiwan, under a MOST grant for the Columbus Program MOST110-2636-M-006-016, National Cheng Kung University, Taiwan, and National Center for Theoretical Sciences, Taiwan. This work was supported partially by the MOST, Taiwan, grant MOST107-2627-E-006-001. This research was supported in part by Higher Education Sprout Project, Ministry of Education to the Headquarters of University Advancement at National Cheng Kung University (NCKU). M.Z.H. acknowledges support from Lawrence Berkeley National Laboratory and the Miller Institute of Basic Research in Science at the University of California, Berkeley in the form of a Visiting Miller Professorship.

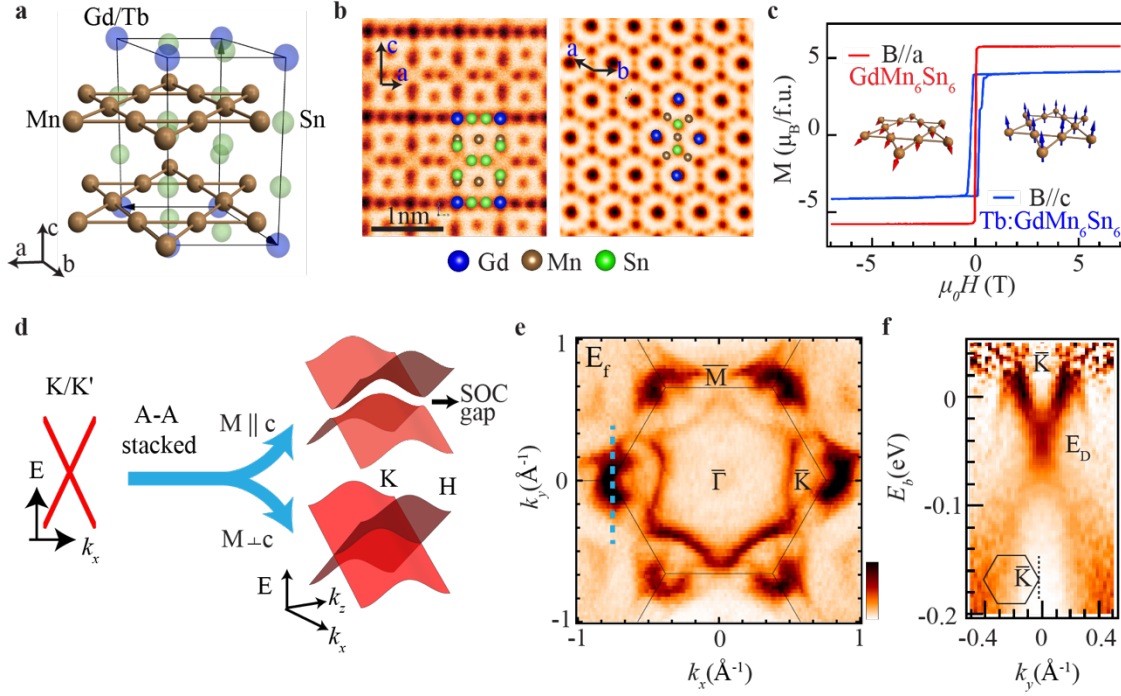


FIG. 1. Structure, magnetism and Dirac crossing in kagome lattice $\text{Tb}_x\text{Gd}_{1-x}\text{Mn}_6\text{Sn}_6$. (a) Crystal structure, emphasizing the A-A stacked Mn kagome lattice. The black lines: side of the conventional unit cell. (b) Scanning transmission electron microscope (STEM) images of side surface (left panel) and top surface (right panel) of GdMn_6Sn_6 , where the conventional unit cell is superimposed on top of the STEM results. (c) Magnetic moment versus in-plane applied magnetic field (red line, on GdMn_6Sn_6) and out-of-plane magnetic field (blue line, $\text{Tb}_{0.2}\text{Gd}_{0.8}\text{Mn}_6\text{Sn}_6$ at $T = 10$ K. f.u.: formula unit). (d) Illustration of the effect of A-A stacking and magnetization direction: tuning Dirac cone of 2D kagome lattice into nodal line along KH direction with magnetization-direction dependent SOC gap. (e) FS map of GdMn_6Sn_6 with (001) termination, taken with 140 eV, horizontal polarized light and at 16 K. The image is obtained by binning within 10 meV around the Fermi level. (f) Renormalized ARPES energy-momentum cut along the dashed line in (e).

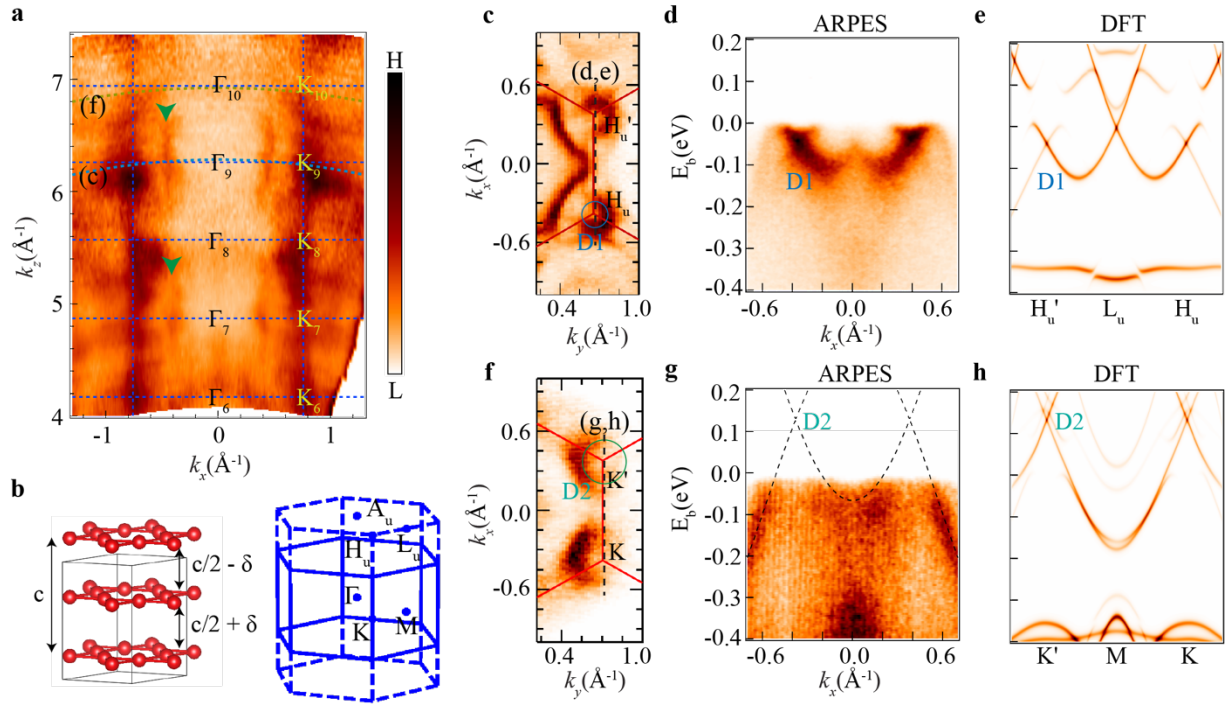


FIG. 2. Photon energy dependence and band unfolding effect of Dirac states. (a) FS map in $k_z - k_x$ plane, showing clear BZ doubling effect of the state marked by the green arrows. Inner potential, $V_0 = 14$ eV. (b) Left: crystal structure with only Mn atoms, which has A-A stacking pattern along c axis with nearly identical interlayer spacing. Right: original BZ (solid line) and doubled BZ (dashed line). (c) and (f) are Fermi surface maps taken at $k_z \approx 9 \frac{2\pi}{c}$ and $k_z \approx 10 \frac{2\pi}{c}$, respectively. The k_z momentum trajectories of two maps are shown as dashed lines in (a). (d) and (g) are energy-momentum cuts taken along the dashed lines in the corresponding FS maps (c) and (f). The dashed line in (g) is the fitting results using single-orbit kagome model. The two Dirac points are labeled with D1 and D2. (e) and (h) are corresponding theoretical calculations, which shows excellent consistency with (d) and (g), respectively.

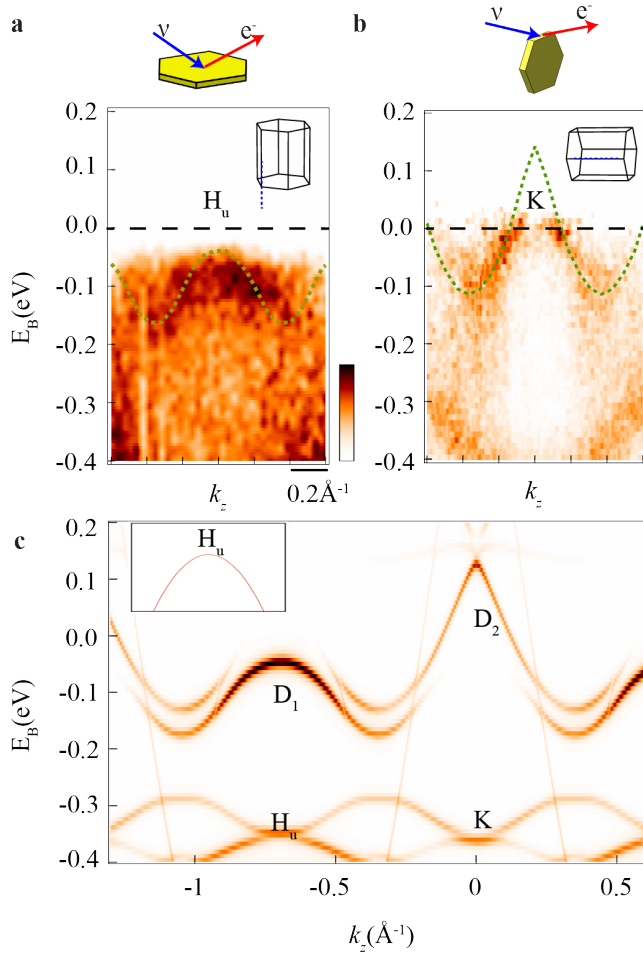


FIG. 3. Strong k_z dispersion of magnetic nodal lines. (a) and (b) are k_z dispersion of the D1 Dirac cones and D2 Dirac cones along K-H direction, respectively. The schematics above the ARPES results show the cleaving plane of each cut. The green dashed lines are the calculation results extracted from (c). The inset in (c) is the zoom-in theoretical band dispersion (without SOC) of D1 Dirac cones near band top, showing the double degeneracy of the nodal line.

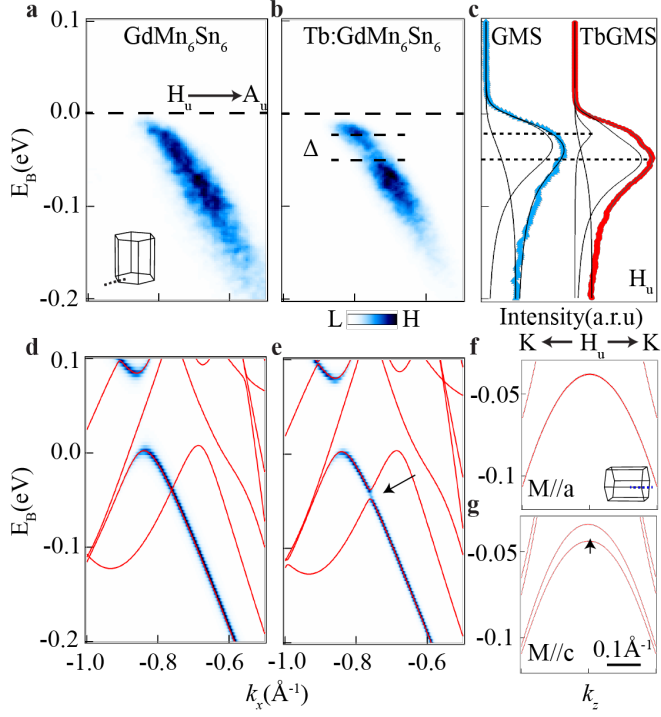


FIG. 4. Magnetic-moment-direction tunable SOC gap of the D1 nodal line. (a) Energy momentum cut along $H_u - A_u$ in the unfolded BZ of $GdMn_6Sn_6$. (b) Analogous to (a), but of $Tb_{0.2}Gd_{0.8}Mn_6Sn_6$. (c) EDCs through the crossing point at H_u (also see Fig. S10). (d-f) Calculated Band dispersion with $M//a$ (d) and $M//c$ (e), for comparison with (a-b). The blue lines are unfolded band calculation. (f-g) Calculated Band dispersion along H_u-K with $M//a$ (f) and $M//c$ (g). The insets in (a) and (g) denote the direction of the cuts in the unfolded BZ.